Nano Research Energy

ISSN 2791-0091 (print); 2790-8119 (online)
https://doi.org/10.26599/NRE.2026.9120272

Research Article

Product selectivity switching in photocatalytic H_2 and H_2O_2 production via carbonized polymer dots loading on carbon nitride hybrids

Mei Han[1] (✉), Zihui Wang[1], Zhihui Ma[2], Xiaotong Yan[1], Xiaodong Yang[1], Xiaoying Hu[1], Lili Wang[1], and Bai Yang[2] (✉)

[1] *School of Materials Science and Engineering, Changchun University, Changchun 130022, China*
[2] *State Key Laboratory of Supramolecular Structure and Materials, College of Chemistry, Jilin University, Changchun 130012, China*

Received: 2 July 2026 / **Revised:** 23 July 2026 / **Accepted:** 4 August 2026 / **Published date:** 22 September 2026

ABSTRACT

Selective regulation of competing photoreduction pathways remains a key challenge in photocatalysis. Most materials that promote one target product often unintentionally accelerate competing side reactions. Here, we demonstrated that carbonized polymer dots (CPDs) served as dual function in graphitic carbon nitride hybrids. By varying the CPDs loading, the continuous increase in hydrogen (H_2) evolution rate was achieved, while hydrogen peroxide (H_2O_2) production was suppressed. The optimal CPDs loading enhanced the H_2 evolution rate by 5.4 times and reduced the H_2O_2 yield by 72%. Mechanistic studies demonstrated that CPDs introduction narrowed the bandgap, promoted charge separation and transfer, and induced a downward shift of the conduction band minimum along with a lowered Fermi level. These energetic modifications weakened the thermodynamic driving force for the two-electron oxygen reduction pathway and steered the reaction toward a four-electron process. This work established CPDs as a versatile platform for reaction pathway regulation and provided a generalizable strategy for product-selective photocatalysis through precise band structure engineering.

KEYWORDS

carbonized polymer dots, graphitic carbon nitride, hydrogen peroxide, photocatalysis, two-electron pathway

1 Introduction

Semiconductor photocatalysis offers a sustainable platform for the conversion of solar energy into chemical feedstocks. It also shows great potential for environmental remediation and the production of high-value-added chemicals [1–3]. Among the diverse range of products, hydrogen (H_2) and hydrogen peroxide (H_2O_2) are particularly valuable [4–6]. Specifically, H_2 can serve as a clean energy carrier, while H_2O_2 is a green oxidant that is widely used in environmental remediation and chemical synthesis [7–11]. Consequently, photocatalytic H_2 evolution reaction (HER) and H_2O_2 generation have attracted widespread research interest [12, 13]. To meet the demand for efficient H_2 and H_2O_2 production, numerous catalyst engineering strategies have been developed. Recent advances have demonstrated the feasibility of simultaneous production via rational catalyst design. For instance, the laser-induced direct overall water splitting system achieved an impressive energy conversion efficiency of light-to-chemical products of 2.1%, yielding H_2 at 2.2 mmol·h^{-1} and H_2O_2 at 65 μM·h^{-1} under irradiation [14]. Similarly, few-layer C_{60} networks and covalent organic frameworks-based photocatalysts with different substituents (–H, –CH_3, and –OH) were reported to enable photocatalytic H_2 evolution and H_2O_2 production reactions [15, 16]. Both Pd/GaN nanowires and Pt-loaded anatase TiO_2 systems have also demonstrated simultaneous solar-driven H_2 and H_2O_2 production, with the latter reaching rates of 7410 and 5096 μmol·g^{-1}·h^{-1}, respectively [17, 18]. These studies collectively illustrated that the rational design of photocatalysts can effectively promote the production rates of H_2 and H_2O_2.

More critically, H_2 is produced directly by proton reduction. In contrast, H_2O_2 can be generated through multiple pathways, including the two-electron ($2e^-$) oxygen reduction reaction (ORR) and the water oxidation reaction [19]. This mechanistic diversity makes photocatalytic H_2O_2 synthesis scientifically attractive. Photosynthesis of H_2O_2 also offers a clean alternative to the energy-intensive anthraquinone process [5, 20]. The present study focuses on the ORR pathway, as it fundamentally governs the efficiency and selectivity of the process. The ORR can proceed via either a $2e^-$ pathway to yield H_2O_2, the valuable chemical feedstock, or a four-electron ($4e^-$) pathway to produce water (H_2O) [12, 19, 21]. To address this, researchers have developed various material

© The Author(s) 2026. Published by Tsinghua University Press. The articles published in this open access journal are distributed under the terms of the Creative Commons Attribution 4.0 International License (http://creativecommons.org/licenses/by/4.0/), which permits use, distribution and reproduction in any medium, provided the original work is properly cited.

Address correspondence to Mei Han, hanm@ccu.edu.cn; Bai Yang, byangchem@jlu.edu.cn

modification strategies. For example, Cu-based single atom catalysts (SACs) supported on WO_3 showed that the Cu(I) oxidation state was more active for 2e⁻ ORR than Cu(II) [22]. By anchoring Cu-based SACs on carbon nanotubes with varying diameters, researchers found that high curvature induced tensile strain on Cu–N bonds, steering the ORR from a 2e⁻ to a 4e⁻ pathway [23].

In addition to SACs, carbon-based materials have emerged as versatile platforms for structural and electronic modulation in photocatalysis [24]. Graphitic carbon nitride (g-C_3N_4) stands out as a promising metal-free photocatalyst for these applications [25, 26]. It offers a suitable bandgap, good stability, and low cost [27, 28]. Nevertheless, the intrinsic activity of pristine g-C_3N_4 is fundamentally limited by the rapid recombination of photogenerated charge carriers and sluggish surface reaction kinetics [29]. To address these drawbacks, researchers have developed various modification strategies. The anchoring of Co and Pt dual sites onto g-C_3N_4 lowered thermodynamic barriers, leading to efficient H_2O_2 photosynthesis in pure water [21]. Furthermore, the integration of concerted proton electron transfer with an S-scheme heterojunction has proven beneficial. A PTA/g-C_3N_4 heterojunction used carboxyl groups as proton relays to facilitate the 2e⁻ ORR [30]. Coupling g-C_3N_4 with carbon-based nanomaterials has proven particularly effective [5, 31–35]. Among them, carbon dots (CDs) and their derivatives (such as carbonized polymer dots, CPDs) have been proven to be effective for enhancing the photocatalytic performance of g-C_3N_4 [29, 32, 36–41]. CPDs have been confirmed to extend the light-responsive range, redistributing of photoinduced electron/hole pairs, and act as efficient electron donors, thereby demonstrating a significant improvement in H_2 generation rates [42].

However, most prior research has aimed to enhance the simultaneous production of H_2 and H_2O_2. It remains unclear how the catalyst structure controls the selectivity between these two pathways. Recent efforts have addressed this challenge through precise molecular-level structural modulation. Interestingly, Yang et al. demonstrated that switching the molecular packing of a donor-acceptor organic photocatalyst from amorphous nanospheres to ordered nanofibers could switch the product selectivity from H_2O_2 to H_2 [43]. In a related effort, photocatalytic selectivity was switched from H_2 (nanofibers) to H_2O_2 (nanoparticles) by pyrene-based aggregates via charge-transfer versus excimer pathways [44]. Beyond morphological control, a donor-acceptor linear polymer semiconductor powder was designed to self-assemble in water via hydrogen-bonding and π-stacking, which enabled efficient photocatalytic H_2O_2 production through the 2e⁻ ORR pathway [45]. The above studies demonstrated that controlling nanoscale aggregation or molecular packing can enable selective switching between photocatalytic H_2 and H_2O_2 production.

Inspired by these researches, we constructed a series of CPDs-modified g-C_3N_4 hybrid photocatalysts with controlled CPDs loadings. The H_2 evolution rate was continuously enhanced and H_2O_2 production was progressively suppressed with increasing CPDs content. This decoupled effect challenges the conventional view that CPDs merely act as universal activity enhancers. The underlying mechanism was elucidated through experimental investigations and density functional theory (DFT) calculations. CPDs not only promoted charge separation but also induced a downward shift of the conduction band minimum of g-C_3N_4. This band alignment change weakened the thermodynamic driving force for the 2e⁻ ORR pathway to H_2O_2. Instead, it favored the 4e⁻ ORR to H_2O. Our findings establish CPDs as dual-function modifiers that can selectively direct competing photoreduction pathways through precise band structure engineering.

2 Experimental

2.1 Materials and methods

All reagents were obtained from commercial suppliers and used without further purification. Citric acid (CA) was purchased from Aladdin. Ethylenediamine (EDA) was obtained from Thermo Fisher Scientific. Urea, potassium hydrogen phthalate ($C_8H_5KO_4$), potassium iodide (KI), and sodium sulfate (Na_2SO_4) were supplied by Sinopharm Chemical Regent. Chloroplatinic acid ($H_2PtCl_6{\cdot}6H_2O$) was purchased from Energy Chemical. Deionized (DI) water (> 18 MΩ·cm) was produced using a Milli-Q system. Other organic solvents were purchased from Beijing Chemical Works.

2.1.1 *Synthesis of polymeric g-C_3N_4*

The polymeric g-C_3N_4 was prepared according to a standard procedure. Typically, 5 g of urea was calcinated at 550 °C for 1 h with a heating rate of 15 °C·min⁻¹ in a muffle furnace under static air. The yellow product was collected, ground, and labeled as PCN.

2.1.2 *Synthesis of CN-CPDs composites*

CPDs was synthesized according to the previous works [37, 42]. In a typical procedure, a certain volume of CPDs solution (x mL, 1 mg·mL⁻¹) was added to 5 g of urea. The mixture was dried at 60 °C in an oven and then calcinated at 550 °C for 1 h with a heating rate of 15 °C·min⁻¹ in a muffle furnace under static air. The obtained product was ground to powder and labeled as CN-CPDs-x, where x = 0.1, 0.5, 1.0, 2.0, or 4.0.

2.2 Characterizations

Transmission electron microscopy (TEM) was performed on a JEM-2100F at an accelerating voltage of 200 kV. Ultraviolet-visible (UV-vis) absorption spectra were recorded on a Shimadzu 3100 spectrophotometer. UV-vis diffuse reflectance spectroscopy (DRS) spectra were obtained on a UV-VIS-NIR spectrophotometer (Lambda 950, Perkinelmer) using $BaSO_4$ powder as the white standard. The Kubelka-Munk function was applied to convert reflectance data to absorption spectra. X-ray diffraction (XRD) patterns were collected on a PANalytical Empyrean diffractometer using Cu Kα radiation (λ = 1.5406 Å) operating at 40 kV and 40 mA. X-ray photoelectron spectroscopy (XPS) was conducted on a Thermo ESCALAB-250Xi spectrometer with monochromatic Al Kα X-ray source. A 300 W Xe lamp (CEL-HXF300, Beijing Ceaulight Technology Co., Ltd.) equipped with a 420 nm cut-off filter served as the light source and was positioned approximately 20 cm from the samples. Fluorescence spectra were acquired on a Hitachi F-7000 spectrophotometer at room temperature. Time-resolved photoluminescence decay spectra were measured on an FLS980 spectrometer (Edinburgh Instruments) with a gated photomultiplier tube. The optical bandgap (E_g) was estimated from the absorption onset. The direct E_g was determined by extrapolating the linear region of the absorption spectrum to the wavelength axis. The calculation followed the equation $E_g = h\upsilon = hc/\lambda$, where h is Planck's constant (6.62607×10^{-34} J·s or 4.135667×10^{-15} eV·s), c is the speed of light (3×10^8 m·s⁻¹), and λ is the wavelength in meters.

2.3 Photocatalytic experiments

2.3.1 *Photocatalytic water splitting for H_2 evolution*

The photocatalytic H_2 evolution activity was evaluated in a closed vacuum reactor under a 300 W Xe lamp with a cut-off filter (λ > 420 nm). In a typical test, the as-prepared catalyst (20 mg) was dispersed in an aqueous TEOA solution (10 vol.%, 50 mL) by sonication. The reactor was evacuated and purged with vacuum to remove air before irradiation, followed by stirring for 20 min. During the irradiation, the suspension temperature was maintained at 6 °C by circulating cooling water and continuously stirred. The evolved H_2 was analyzed every 30 min using an online gas chromatograph (GC-7920) equipped with a thermal conductivity detector (TCD) and high-purity N_2 as the carrier gas. The Pt cocatalyst (2 wt.%) was deposited *in situ* via photodeposition by adding a calculated amount of $H_2PtCl_6{\cdot}6H_2O$ aqueous solution to the reaction mixture prior to irradiation.

2.3.2 *Photocatalytic reduction of oxygen to H_2O_2*

The photocatalytic H_2O_2 production activity was evaluated using isopropanol (IPA) as a sacrificial agent. In a typical test, 10 mg of the as-synthesized photocatalyst was dispersed in IPA solution (10 vol.%, 50 mL) by ultrasonication for 30 min. The suspension was then stirred in the dark for 30 min with continuous O_2 bubbling to reach absorption-desorption equilibrium. The reaction was conducted in a quartz glass reactor equipped with a circulating water system to maintain the temperature at 25 °C. The suspension was then irradiated with visible light from a 300 W Xe lamp equipped with a 420 nm cutoff filter. The lamp was positioned 10 cm from the reactor. Continuous magnetic stirring and cooling water circulation were applied throughout the experiment. During illumination, aliquots of 3 mL were withdrawn every 10 min and filtered through a 0.22 μm membrane to remove the catalyst particles. The H_2O_2 concentration was determined by the iodometric method [46]. In this analysis, 1 mL of $C_8H_5KO_4$ (0.1 mol·L^{-1}) and 1 mL of KI (0.4 mol·L^{-1}) were added to the filtrate. The mixture was allowed to stand for 30 min. Under acidic conditions, H_2O_2 oxidized iodide ions (I^-) to generate triiodide ions (I_3^-) according to the reaction $H_2O_2 + 3I^- + 2H^+ \rightarrow I_3^- + 2H_2O$. The formed I_3^- exhibited a characteristic absorption peak at around 350 nm. Its concentration was determined by UV-vis spectroscopy based on the absorbance at this wavelength. The amount of H_2O_2 produced during each reaction was then calculated from the standard curve.

2.3.3 *Photocatalytic H_2O_2 splitting*

The photocatalytic decomposition of H_2O_2 was carried out in a closed gas circulation system. In a typical test, 50 mg of the catalyst was added to a quartz reactor containing 50 mL of aqueous solution, along with 100 μL of H_2O_2 and 7 mL of phosphoric acid solution. Prior to illumination, the reactor was evacuated and purged to remove air, followed by stirring for 20 min. During irradiation, the temperature was maintained at 6 °C by circulating cooling water, and the suspension was continuously stirred. The evolved O_2 was analyzed every 30 min using an online gas chromatograph (GC-7920) equipped with a thermal conductivity detector (TCD) and high-purity N_2 as the carrier gas.

2.3.4 *Photoelectrochemical measurements*

The photoelectrochemical properties were measured using a standard three-electrode system with an electrochemical workstation (CHI660E, Chenhua Instruments Co., China). A saturated calomel electrode (SCE) and a platinum wire were used as the reference and counter electrodes, respectively. The working electrode was a catalyst film coated on an ITO glass substrate. The electrolyte was an aqueous Na_2SO_4 solution (0.1 mol·L^{-1}). A 300 W Xe lamp equipped with a 420 nm cut-off filter served as the visible light source. The measurements included photocurrent response, electrochemical impedance spectroscopy (EIS), and Mott-Schottky curves.

3 Results and discussion

3.1 Photocatalytic performance

The photocatalytic activity of the CN-CPDs-*x* hybrids (*x* = 0, 0.1, 0.5, 1.0, 2.0, and 4.0, denoting the added CPDs solution volume in mL) was assessed under visible light (λ > 420 nm). Photocatalytic water splitting for H_2 evolution was conducted with TEOA as a sacrificial agent and Pt as a co-catalyst. Meanwhile, photocatalytic O_2 reduction for H_2O_2 production was carried out under O_2 saturation with IPA as a hole scavenger. As displayed in Fig. 1(a) and summarized in Table S1 in the Electronic Supplementary Material (ESM), the evolution rates of H_2 and H_2O_2 exhibited distinct opposite trends. The pristine PCN showed an H_2 evolution rate of 440.9 μmol·g^{-1}·h^{-1}. With the introduction of CPDs, the H_2 evolution rates increased progressively. For the CN-CPDs-0.1 sample, the rate reached 1178.8 μmol·g^{-1}·h^{-1}. Further increasing the CPDs loading to *x* = 0.5 and *x* = 1.0 gave rates of 1284.1 and 1489.4 μmol·g^{-1}·h^{-1}, respectively. The optimal performance was achieved over CN-CPDs-2.0, with a rate of 2826.0 μmol·g^{-1}·h^{-1}. This value was approximately 4.4 times higher than that of pristine PCN. Such a substantial enhancement clearly demonstrated that appropriate CPDs incorporation effectively promoted the photocatalytic activity. It was noteworthy that the H_2 evolution rate exhibited a moderate increase from CN-CPDs-0.1 to CN-CPDs-1.0, while a dramatic enhancement was observed for CN-CPDs-2.0. The linear fitting with R^2 = 0.995 for PCN, CN-CPDs-1.0, and CN-CPDs-2.0 confirmed a systematic enhancement trend for H_2 evolution, as shown in Fig. 1(b). The moderate increase at low loadings with *x* < 1.0 was attributed to the progressive but insufficient improvements in light absorption with bandgap narrowing and charge separation with decreased lifetime limited by the number of electron transfer junctions between CPDs and g-C_3N_4. The detailed characterization data supporting these observations are presented in the following sections. When the loading reached *x* = 2.0, the CPDs nanoparticles form a more effective surface modification layer that maximized electron extraction and transfer from g-C_3N_4 to the Pt cocatalyst, resulting in the dramatic enhancement of H_2 evolution. However, when the CPDs loading was further increased to *x* = 4.0, the H_2 evolution rate decreased to 1091.1 μmol·g^{-1}·h^{-1}. This decline was attributed to the aggregation of excess CPDs, which might shield the active sites of the host photocatalyst.

In contrast to the H_2 evolution trend, the H_2O_2 production rate decreased monotonically with increasing CPDs loading. The pristine PCN exhibited an H_2O_2 evolution rate of 1704.2 μmol·g^{-1}·h^{-1}. With the addition of CPDs, the H_2O_2 yields were significantly lower than that of PCN. CN-CPDs-4.0 showed the lowest activity, with a rate of only 476.6 μmol·g^{-1}·h^{-1}. This value corresponded to a 72.0% reduction compared to pristine PCN. As observed, the H_2O_2 production rate displayed a distinct two-stage dependence on CPDs loading, as shown in Fig. 1(b). At lower loadings (*x* < 1.0), a linear correlation was observed between the H_2O_2 rate and

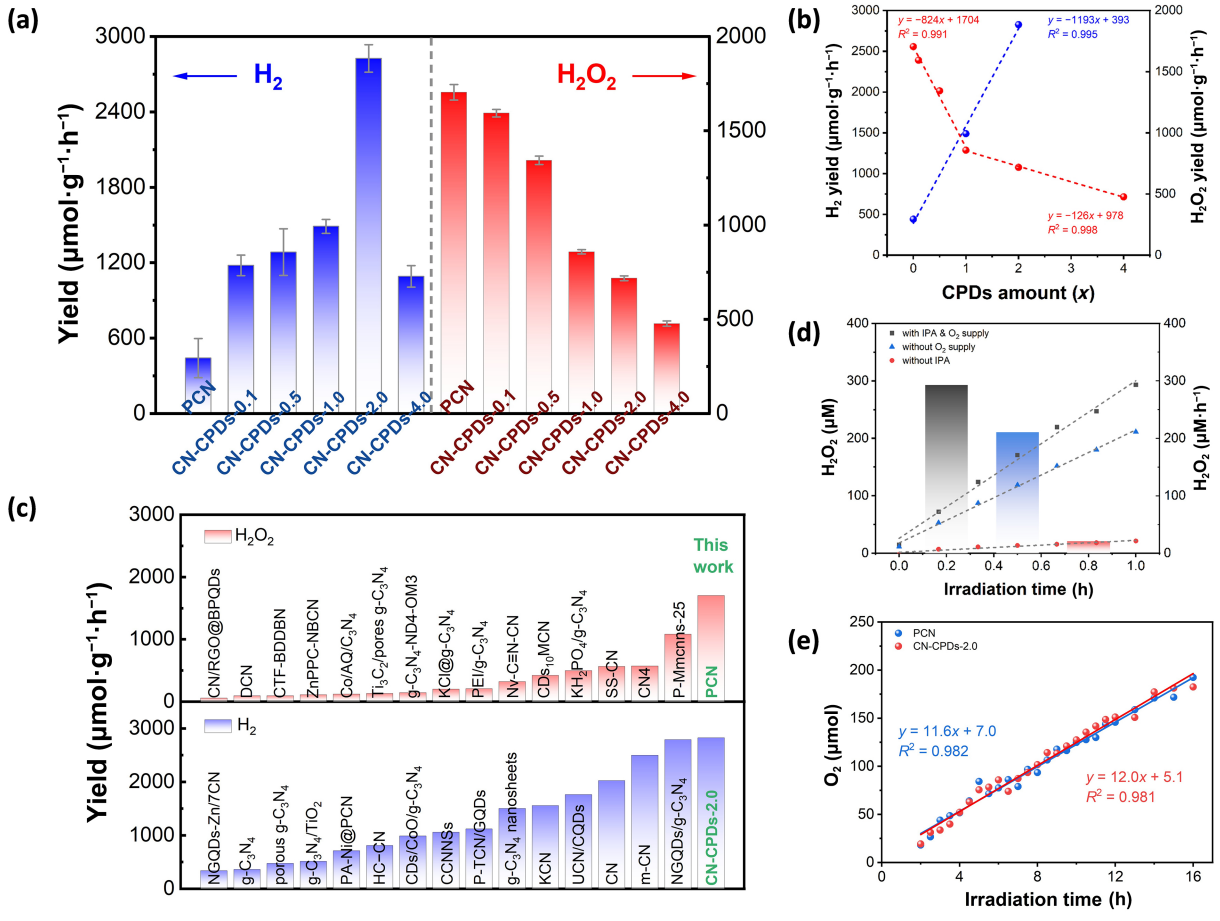


Figure 1 Photocatalytic performance. (a) Photocatalytic H_2 (left) and H_2O_2 (right) evolution performance of the CN-CPDs-*x* series. (b) Photocatalytic H_2 and H_2O_2 production rates and the corresponding linear fits. (c) Comparison for H_2 and H_2O_2 activities with recently reported g-C_3N_4-based photocatalysts (see Tables S2 and S3 in the ESM for details). (d) Photocatalytic H_2O_2 production under various conditions. (e) Photocatalytic H_2O_2 splitting to O_2 over PCN and CN-CPDs-2.0.

the CPDs amount, described by the equation $y = -824x + 1704$ (R^2 = 0.991). The steep negative slope of −824 indicated a high sensitivity of the photocatalytic performance to the CPDs loading in this region. When the loading exceeded x = 1.0, the linear relationship shifted to a milder slope, fitted by the equation y = −126x + 978 (R^2 = 0.998). This two-stage behavior suggested that different mechanistic factors might dominate at low and high CPDs loadings. The attenuation rate moderated significantly to a gentler slope of −126. This slope value was reduced by 85% compared to that in the low-loading region, implying improved catalytic stability at higher CPDs loading levels. These results underscored the critical role of CPDs loading in modulating the photocatalytic performance. The observed variations originated from multiple factors, including changes in light absorption ability, charge transfer efficiency, separation kinetics, and reduction capacity of the catalysts, all of which were dependent on the CPDs content. This finding also highlighted the importance of optimizing co-catalyst loading to balance the reaction efficiency. It should be noted that the H_2 and H_2O_2 production activities were evaluated in separate reaction systems with different sacrificial agents and atmospheres, as required by the distinct reaction mechanisms. The opposing trends observed in these independent systems indicated that CPDs loading can selectively modulate the material toward either proton reduction or oxygen reduction, suggesting a product selectivity switching capability of the hybrid photocatalyst. Notably, the CN-CPDs-2.0 and PCN samples outperformed most of the previously reported g-C_3N_4-based photocatalysts for H_2 and H_2O_2 production (Fig. 1(c); detailed data were provided in Tables S2 and S3 in the ESM). This work presented a unique case in which a single carbon nitride hybrid system could selectively produce either H_2 or H_2O_2, depending on the CPDs loading.

Three controlled experiments were conducted to investigate the ORR mechanism. Condition (i) was the standard system with IPA as a hole sacrificial agent and continuous O_2 bubbling. Condition (ii) was an anoxic system with IPA added but without O_2 bubbling. Condition (iii) was a scavenger-free system with continuous O_2 supply but without IPA. The corresponding H_2O_2 production rates over CN-CPDs-0.1 catalyst under these conditions were presented in Fig. 1(d). Under condition (i), the H_2O_2 yield reached 293 μM·h^{-1}. When the O_2 supply was interrupted in condition (ii), the H_2O_2 production rate decreased to 211 μM·h^{-1}, corresponding to a 28% reduction. This was attributed to the limited dissolved O_2 concentration in water, which was less than 8 mg·L^{-1} at 25 °C. The remaining ORR activity indicated that dissolved O_2 participated in the 2e$^-$ ORR pathway to generate H_2O_2, following the reaction $O_2 + 2H^+ + 2e^- \rightarrow H_2O_2$. The continuous O_2 supply was maintained to ensure adequate reactant availability for the ORR stoichiometry. Meanwhile, the formation rate of reactive oxygen species, including superoxide radicals ($\cdot O_2^-$) was promoted. These radicals were recognized as key intermediates for H_2O_2 generation. The result confirmed that the oxygen atoms in the generated H_2O_2 were derived directly from the supplied O_2. Under reaction condition (iii), the H_2O_2

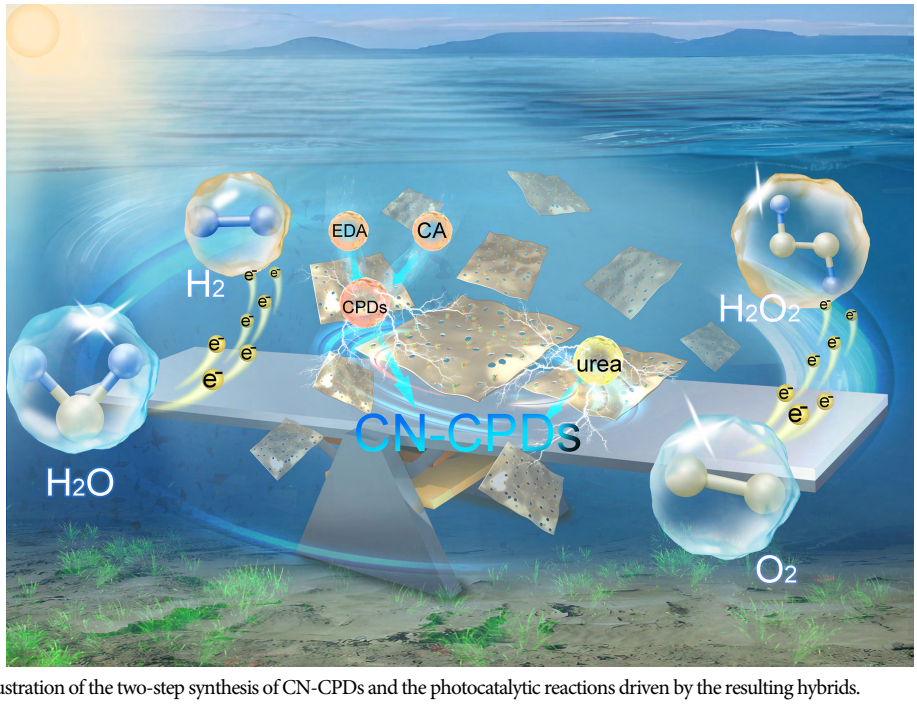
production rate was sharply decreased to 21 μM·h^{-1}. This value corresponded to a 93% reduction relative to the standard system. This significant decrease was attributed to the absence of IPA. IPA was employed as a hole scavenger in the standard system. In the presence of IPA, electrons were donated to the valence band (VB), and the recombination of photogenerated carriers was inhibited. As a result, more electrons were retained in the conduction band (CB) for O_2 reduction. In addition, the consumption of holes by IPA also reduced the oxidative decomposition of H_2O_2 by active holes. The activity difference between condition (i) and condition (iii) was approximately 14-fold. This comparison highlighted the critical role of hole scavenging in suppressing charge carrier recombination and enhancing the H_2O_2 yield.

Further experiments were performed to determine whether the decreased H_2O_2 production rate originated from its decomposition. The photocatalytic decomposition of H_2O_2 was therefore conducted under identical conditions. During the reaction, continuous O_2 evolution was detected, while no H_2 was observed. Therefore, the decomposition rate of H_2O_2 could be evaluated by monitoring the O_2 generation rate, according to the reaction $2H_2O_2 \rightarrow O_2 + 2H_2O$. As shown in Fig. 1(e), the O_2 evolution rates over PCN and CN-CPDs-2.0 were 11.6 and 12.0 μmol·h^{-1}, respectively, after 16 h of irradiation. The difference between the two samples was negligible. These results effectively excluded the possibility of rapid H_2O_2 decomposition after its formation. Thus, the suppressed H_2O_2 yield observed on CN-CPDs-2.0 was attributed to inhibited formation rather than to accelerated decomposition.

3.2 Synthesis and characterization

A series of CN-CPDs hybrid catalysts with varying CPDs loadings were prepared using a two-step approach, as illustrated in Scheme 1. Urea was employed as the precursor for the polymerization of the g-C_3N_4 network. The as-synthesized CPDs solution was mixed with urea under controlled temperature conditions. The mixture was then subjected to a homogeneous thermal polymerization process, and the CN-CPDs catalysts were thereby obtained.

The morphologies and microstructures of PCN and CN-CPDs were characterized by TEM and SEM. Figure S1 in the ESM revealed a typical two-dimensional lamellar structure for all samples, with loosely stacked sheet edges. The lamellar morphology was preserved in the CN-CPDs hybrids even at the highest CPDs loading (x = 4.0). This observation suggested that the introduction of CPDs did not substantially alter the bulk morphology of the g-C_3N_4 matrix. As shown in Fig. 2(a), the PCN sample prepared by direct calcination of urea exhibited a hierarchical morphology assembled with an irregular two-dimensional porous lamellar structure. This morphology was consistent with the typical layered structure of g-C_3N_4. The loading of CPDs was controlled by adjusting the amount of CPDs solution added during the synthesis. At a low CPDs loading (CN-CPDs-0.1), the basic lamellar framework was retained after the copolymerization of CPDs. No distinct CPDs nanoparticles were observed in this sample (Fig. S2(a) in the ESM). When the CPDs loading was increased to CN-CPDs-0.5, discrete CPDs nanoparticles became visible at the edges of the g-C_3N_4 sheets. These nanoparticles exhibited diameters of 2–5 nm, as shown in the HRTEM image in Fig. 2(b). At higher CPDs contents (CN-CPDs-1.0, CN-CPDs-2.0, and CN-CPDs-4.0), a more pronounced distribution of CPDs nanoparticles was observed (Fig. 2(c) and Figs. S2(b) and S2(c) in the ESM). These findings provided compelling evidence for the successful incorporation of CPDs onto the g-C_3N_4 sheets, with the density of the attached CPDs increasing progressively with the loading amount. As shown in Fig. 2(d), two distinct diffraction peaks were observed in the XRD patterns. A small peak at 13.1° was assigned to the (100) plane, corresponding to the in-plane structural packing of the heptazine units, while the strong peak at around 27.5° was indexed to the (002) plane, which resulted from the interlayer stacking of the g-C_3N_4 sheets. It was therefore concluded that the hybrid catalysts retained the original crystalline structure. Consequently, the change in photocatalytic performance was attributed to surface/edge modification rather than to a change in the bulk structure. In addition, elemental analysis was further performed to determine the composition of the synthesized samples. As presented in Table S4 in the ESM, the carbon-to-nitrogen ratio



Scheme 1 Schematic illustration of the two-step synthesis of CN-CPDs and the photocatalytic reactions driven by the resulting hybrids.

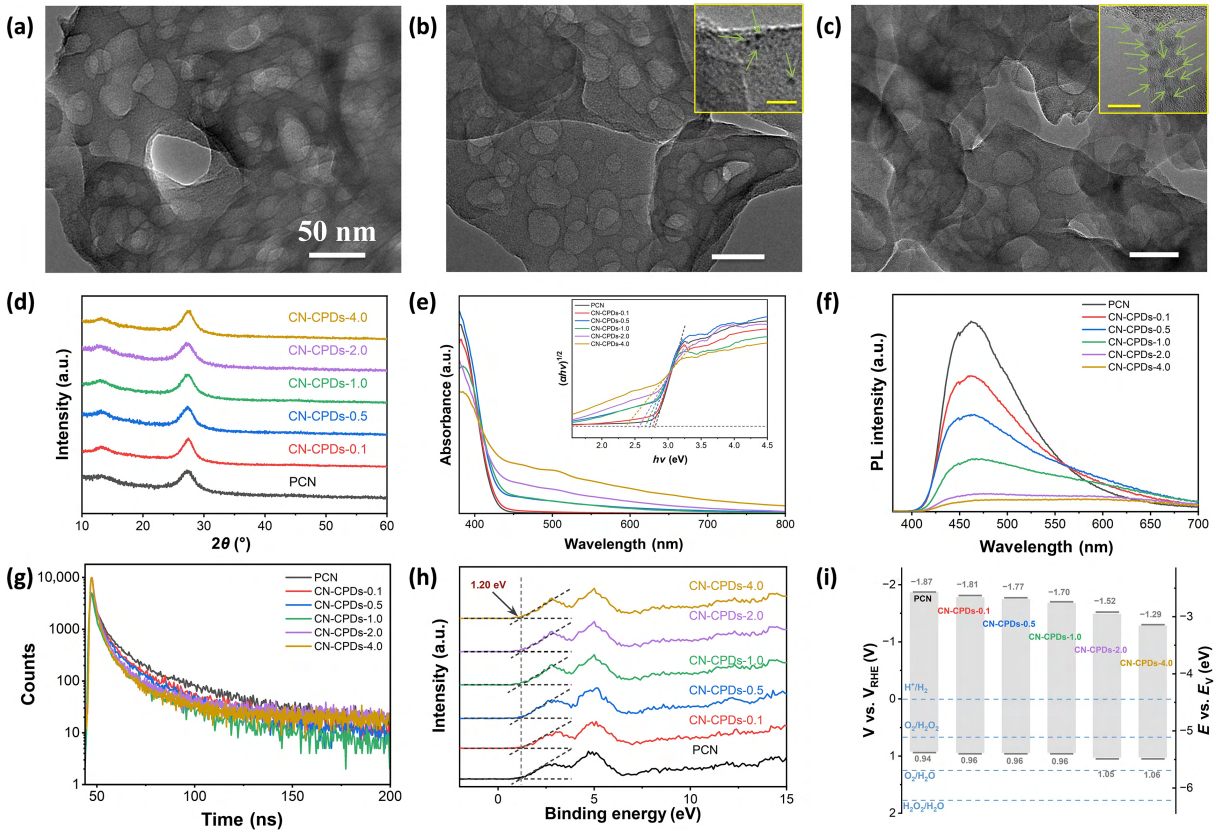


Figure 2 The structural, optical, and electronic properties of the prepared samples. TEM images of (a) PCN, (b) CN-CPDs-0.5, and (c) CN-CPDs-1.0, respectively. Insets: HRTEM images showing the loading of CPDs, in which the scale bars are 10 nm. The green arrows are the guide for the eyes to follow the CPDs. (d) The XRD patterns. (e) UV-vis DRS spectra and the corresponding Tauc plots of $(\alpha h\nu)^{1/2}$ versus photon energy for band gap estimation. (f) PL spectra recorded at an excitation wavelength of 365 nm. (g) Time-resolved transient PL decay curves. (h) VB-XPS spectra. (i) The band structure diagram derived from the combined optical and VB-XPS data.

(C/N) remained approximately 0.66 for all samples, based on the measured C and N contents. This result confirmed that the tri-*s*-triazine framework was preserved throughout the thermal treatment.

3.3 Mechanistic insights

The CPDs loading was found to play a critical role in tuning the photocatalytic activity of the CN-CPDs-*x* hybrids, giving rise to a distinct trade-off between H_2 and H_2O_2 production. A rate of 2826.0 μmol·g^{-1}·h^{-1} was achieved for H_2 evolution over CN-CPDs-2.0, which was 5.4 times that of pristine PCN (440.9 μmol·g^{-1}·h^{-1}). In contrast, the H_2O_2 production rate decreased from 1704.2 to 476.6 μmol·g^{-1}·h^{-1} with increasing CPDs content. This contrasting behavior suggested distinct mechanism for H_2 and H_2O_2 production. The enhanced H_2 evolution rates were attributed to the synergistic effects of improved light-harvesting and charge separation efficiency, while the suppressed H_2O_2 yield may result from competing reaction pathways.

3.3.1 *Light absorption*

The photophysical properties of the g-C_3N_4 matrix were significantly modified by the incorporated CPDs, owing to their light-harvesting capability. As shown in Fig. 2(e), the CN-CPDs-*x* samples exhibited a notable redshift at the absorption edge in the UV-vis DRS spectra, along with enhanced absorption in the visible to near-infrared region. This enhancement was ascribed to the structural features of CPDs, particularly the polymeric shell that broadened the light-harvesting range. Meanwhile, the conjugated sp^2 domains and the surface polymer-like groups facilitated light absorption through π-π* and n-π* electronic transitions. Estimated from the UV-vis DRS data via the Kubelka-Munk method, the optical E_g values were obtained as 2.81 eV (PCN), 2.77 eV (CN-CPDs-0.1), 2.73 eV (CN-CPDs-0.5), 2.66 eV (CN-CPDs-1.0), 2.57 eV (CN-CPDs-2.0), and 2.35 eV (CN-CPDs-4.0), respectively. Overall, the progressive narrowing of E_g with increasing CPDs content was consistent with the enhanced visible-light absorption and the observed change in photocatalytic selectivity.

3.3.2 *Charge separation and transfer*

The separation and transfer of photogenerated charge carriers (electron-hole pairs) are key determinants of photocatalytic performance. The carrier transition behavior of different samples under 365 nm excitation wavelength was first studied by PL spectroscopy. A distinct emission peak at 460 nm was observed for PCN (Fig. 2(f)). This peak was attributed to the recombination of photogenerated charge carriers. Upon the incorporation of CPDs, the PL intensity was substantially reduced, indicating suppressed radiative recombination. This result confirmed that CPDs acted as electron donors after photoexcitation, thereby enhancing the efficiency of photogenerated charge separation. In addition, time-resolved transient PL decay spectra (Fig. 2(g)) were obtained. The average lifetimes (τ_{AVE}) obtained from triple-exponential decay fitting were listed in Table S5 in the ESM. With increasing CPDs content, a progressive decrease in τ_{AVE} was observed, from 24.4 ns for PCN to 5.9 ns for CN-CPDs-4.0. The progressive decrease in

lifetime with increasing CPDs loading indicated enhanced charge transfer kinetics.

These results highlighted several key functions of CPDs. First, broadband light harvesting was enhanced, especially in the visible region. Second, charge separation was promoted through interface engineering, achieving a balance between photon utilization and recombination loss. Third, electron transfer to protons ($2H^+ + 2e^- \rightarrow H_2$) was facilitated, a process in which proton reduction was dominated by electrons and H_2 production was driven by CPDs.

3.3.3 *Band structure*

Furthermore, the electronic modulation induced by CPDs was quantitatively characterized by Mott-Schottky analysis at different frequencies. As shown in Fig. S3 in the ESM, all samples exhibited a positive slope in the Mott-Schottky plots, confirming their n-type semiconductor characteristics. The flat-band potentials (E_{fb}) were determined by extrapolating C^{-2} to zero. The E_{fb} values were −0.50, −0.48, −0.48, −0.48, −0.39, and −0.38 V (*vs.* SCE), corresponding to −0.26, −0.24, −0.24, −0.24, −0.15, and −0.14 V versus RHE. For n-type semiconductors, the E_{fb} approximates the Fermi level (E_F). Quantitative analysis revealed that the incorporation of CPDs induced a downward shift of the Fermi level by 0.12 eV (see Eq. (1) for the calculation). This shift indicates an enhanced electron-withdrawing capability of the modified material.

$$\Delta E_F = -e\Delta E_{fb} = -0.12\ \text{eV} \quad (1)$$

The optical and electronic structure evolution upon CPDs integration was quantitatively probed by UV-vis DRS and XPS valence band spectroscopy (VB-XPS). From the VB-XPS data (Fig. 2(h)), the VB edge of PCN was determined to be 1.20 eV versus the vacuum level [29]. The CB minima were then calculated using $E_{CB} = E_{VB} - E_g$, based on the optical E_g values. The resulting band edge positions were summarized in Fig. 2(i). A progressive downward shift of the CB edge was observed as the CPDs loading increased. This shift altered the thermodynamic landscape of the photocatalytic system, while the reduction potentials of CN-CPDs were still sufficient to drive the $2e^-$ ORR pathway. As a consequence, H_2O_2 formation was thermodynamically disfavored.

3.3.4 *Theoretical calculations*

DFT-based theoretical calculations of the band gap structure and density of states (DOS) elucidated the origin of the pathway switching at the atomic level. The structure of PCN was modeled as a two-dimensional periodic melon-like polymer (Fig. 3(a)). This polymer consisted of heptazine units bridged by sp^2-hybridized carbon atoms, with terminal $-NH_2$ groups attached to the framework. To represent the CPDs-modified carbon nitride (Fig. 3(b)), the surface molecule on CPDs, 1,2,3,5-tetrahydro-5-oxo-imidazo[1,2-α]pyridine-7-carboxylic acid (IPCA) was incorporated into the g-C_3N_4 framework as a surface model [42]. The incorporation of CPDs was accompanied by localized structural distortions, as evidenced by the presence of oxygen-containing functional groups (indicated by red atoms), and altered bonding configurations. These DFT-constructed models were then employed to investigate the electronic structure modifications induced by CPDs functionalization.

The band structure of PCN was calculated along the high-symmetry path Γ–X–Γ–Z–Γ in the Brillouin zone (Fig. 3(c)). A direct bandgap of 1.18 eV was obtained, with both the conduction band minimum (CBM) and valence band maximum (VBM) located at the Γ point. It should be noted that the absolute bandgap values obtained from DFT-PBE calculations are systematically underestimated compared with experimental optical bandgaps, a well-known limitation of GGA-type functionals. Nevertheless, the relative trends upon CPDs modification remained reliable and qualitatively consistent with experimental results. The band dispersion was spin-independent, suggesting the absence of inherent spin polarization in the pristine phase. Upon CPDs modification, a spin-polarized electronic configuration was revealed in the band structure (Fig. 3(d)). The spin-up (black curves) and spin-down (red curves) channels exhibited distinct energy dispersions, resulting in significant spin splitting near the Fermi level (set as 0 eV). Impurity states were introduced near the Fermi level by this modification, which narrowed the bandgap to 0.83 eV.

The total DOS of PCN exhibited typical semiconductor characteristics near the Fermi level (set at 0 eV, Fig. 3(e)). For the CPDs-modified carbon nitride (CN-CPDs), spin-polarized DOS calculations revealed a pronounced asymmetry between the spin-

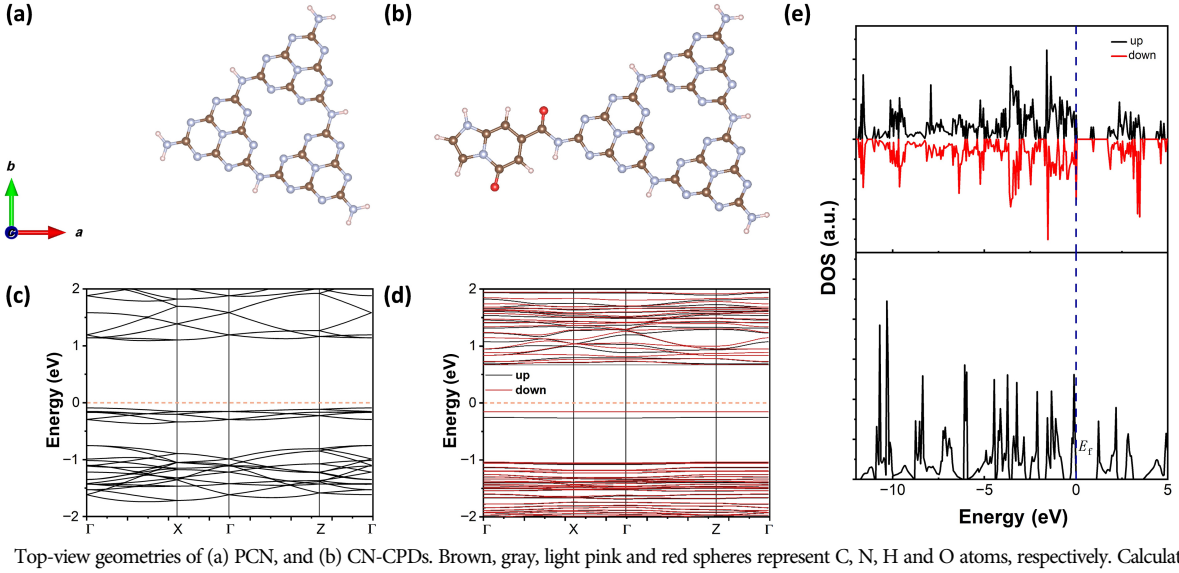


Figure 3 Top-view geometries of (a) PCN, and (b) CN-CPDs. Brown, gray, light pink and red spheres represent C, N, H and O atoms, respectively. Calculated band structure of (c) PCN and (d) CN-CPDs. (e) Corresponding DOS. The Fermi level is set at 0 eV (blue dashed line). The black and red lines denote the spin-up and spin-down channels, respectively.

up and spin-down channels near the Fermi level, along with sharp peak features. From these observations, CPDs modification was inferred to introduce organic fragments and defects within the forbidden band, thereby generating localized electronic states. The emergence of these impurity states altered the direct bandgap of pristine g-C_3N_4. A spin-resolved band structure also suggested enhanced spin-dependent electronic transport. The calculated DOS of the CPDs-modified model (with IPCA incorporated) showed the presence of gap states and a narrowed bandgap, which was consistent with the experimental observations.

3.3.5 *Competing ORR pathways*

The ORR proceeds via two primary competing thermodynamic pathways. The 2e⁻ ORR pathway produces H_2O_2 following the reaction $O_2 + 2e^- + 2H^+ \rightarrow H_2O_2$, while the 4e⁻ ORR pathway yields H_2O via $O_2 + 4e^- + 4H^+ \rightarrow 2H_2O$ [47]. These two routes were illustrated in Fig. 4(a). The corresponding standard equilibrium potentials (U^0) and the general reaction sequences were described below. The asterisk (*) denoted an active site on the catalyst surface [19].

2e⁻ ORR pathway :

$$O_2 + 2(H^+ + e^-) \rightarrow H_2O_2\ U^0 = 0.68\ \text{V}$$

$$\bullet + O_2 + H^+ + e^- \rightarrow {}^*OOH$$

$${}^*OOH + H^+ + e^- \rightarrow H_2O_2 + {}^*$$

4e⁻ ORR pathway :

$$O_2 + 4(H^+ + e^-) \rightarrow 2H_2O\ U^0 = 1.23\ \text{V}$$

$$\bullet + O_2 + H^+ + e^- \rightarrow {}^*OOH$$

$$OOH + H^+ + e^- \rightarrow H_2O + O$$

$${}^*O + H^+ + e^- \rightarrow {}^*OH$$

$${}^*OH + H^+ + e^- \rightarrow H_2O + {}^*$$

The catalytic selectivity between these pathways is governed by the adsorption free energies of key ORR intermediates, including

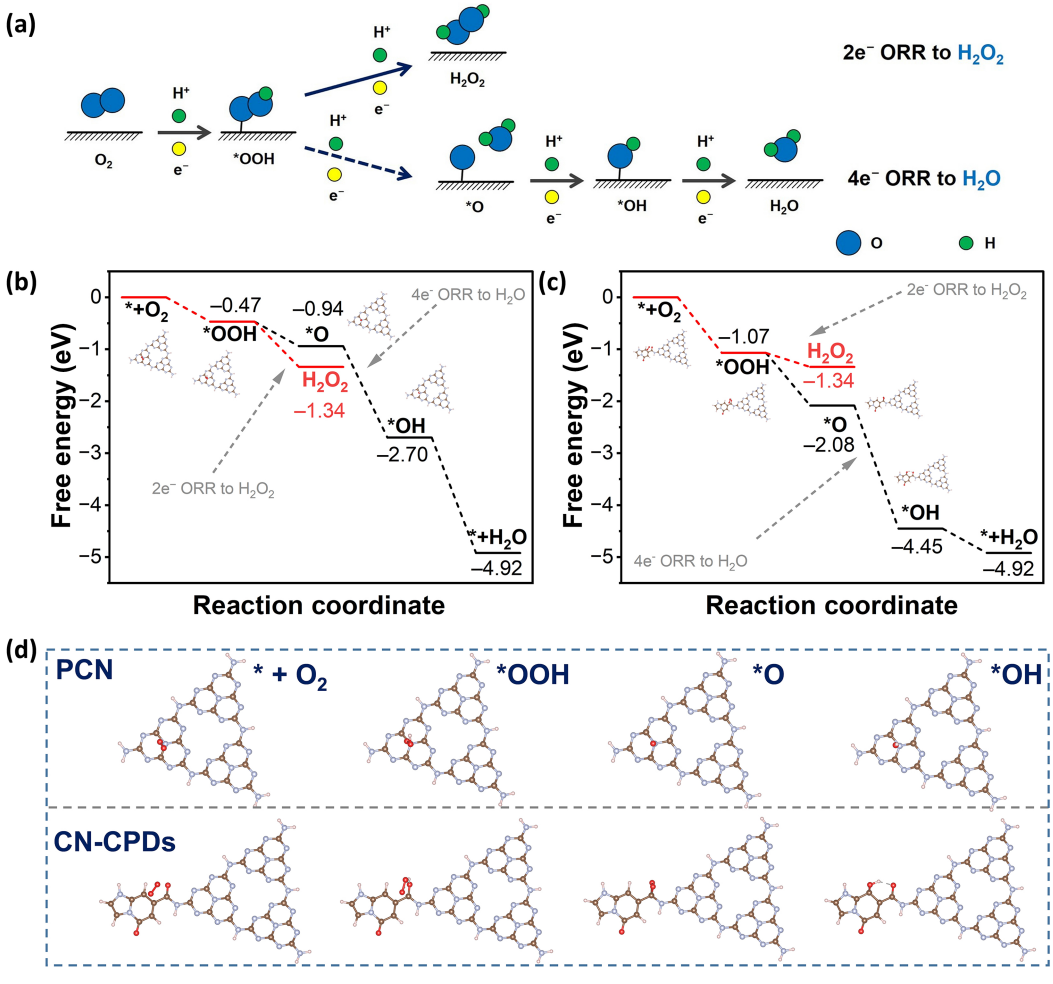


Figure 4 The ORR pathways and the corresponding free energy profiles. (a) Schematic illustration of the two primary ORR routes. The 2e⁻ pathway produced H_2O_2, while the 4e⁻ pathway yielded H_2O. Key adsorbed intermediates along the reaction coordinate were highlighted, including *OOH, *O, and *OH. In the atomic color scheme, brown, gray, light pink and red spheres represent C, N, H and O atoms, respectively. Gibbs free energy profiles for ORR on (b) pristine PCN and (c) CN-CPDs active sites, respectively. All energy values were given in electron volts (eV). The profiles illustrated the effect of CPDs functionalization on the reaction selectivity. (d) The optimized adsorption configurations of the key ORR intermediates on the catalyst surfaces. The adsorption sites for *OOH, *O, and *OH were identified on both PCN and CN-CPDs.

*OOH, *O, and OH. To elucidate this effect, Gibbs free energy profiles for these intermediates on pristine PCN and CPDs-modified CN-CPDs were constructed using DFT-based calculations. A systematic evaluation of oxygen molecule adsorption energies (E_{ads}) at various active sites was performed, as shown in Fig. S4 in the ESM. For PCN, three distinct adsorption configurations were analyzed. The corresponding E_{ads} values were −0.129, −0.105, and −0.094 eV, respectively. The most favorable configuration exhibited an E_{ads} of −0.129 eV. This indicated a preferential oxygen interaction at specific nitrogen atoms in the heptazine ring. For CN-CPDs, five adsorption configurations were identified. The E_{ads} values were −0.256, −0.174, −0.170, −0.157, and −0.134 eV, respectively. The optimal adsorption site for CN-CPDs yielded an E_{ads} of −0.256 eV. This value is substantially more negative than that of PCN, highlighting the enhanced oxygen-binding affinity induced by the CPDs modification.

The free energy profiles provided a clear mechanistic explanation for the observed selectivity, as shown in Figs. 4(b) and 4(c). The adsorption configurations of the key intermediates on the catalyst surfaces were further examined, as presented in Fig. 4(d). On PCN, the *OOH, *O, and *OH intermediates were preferentially adsorbed at the nitrogen sites of the heptazine units. On CN-CPDs, the adsorption behavior was significantly altered by the presence of CPDs. The oxygen-containing functional groups of CPDs introduced additional binding interactions with the intermediates. Consequently, the adsorption geometries and binding energies of *O and *OH were distinctly different between the two catalysts. These differences in adsorption energetics were responsible for the shifted reaction pathway from $2e^-$ to $4e^-$ ORR. For unmodified PCN, the desorption of *OOH to form H_2O_2 exhibited a relatively low energy barrier. This low barrier favored the $2e^-$ pathway and promoted selective H_2O_2 production. In contrast, the subsequent steps of the $4e^-$ pathway, namely *OOH → *O and *O → *OH, involved substantial energy decreases. These large energy drops rendered the complete $4e^-$ reduction to H_2O thermodynamically less favorable on PCN. Therefore, the $2e^-$ pathway was thermodynamically preferred on this material.

In the case of CN-CPDs, the energy landscape differed markedly from that of PCN. Lower energy minima were observed for the *OOH → *O and *O → *OH steps. This reflected enhanced stabilization of the *O and *OH intermediates on the modified surface. Consequently, the energy barriers along the $4e^-$ pathway were effectively reduced. Furthermore, the *OH desorption to H_2O on CN-CPDs was slightly less exothermic than that on PCN. This moderated energy release optimized the adsorption-desorption balance of *OH, which lowered the theoretical overpotential and prevented excessive *OH coverage that could hinder catalytic activity. DFT calculations and reaction pathway analysis were employed to elucidate the origin of the suppressed H_2O_2 yield upon CPDs incorporation. The results revealed that CPDs modification systematically modulated the adsorption free energies of the ORR intermediates and flattened the free energy profile along the $4e^-$ pathway. As a result, the competing $2e^-$ ORR pathway to H_2O_2 was suppressed, while the complete $4e^-$ reduction of O_2 to H_2O was thermodynamically stabilized on CN-CPDs. This mechanistic understanding established a clear structure-activity relationship and confirmed the critical role of CPDs in directing the ORR selectivity.

In summary, the ORR selectivity in photocatalytic H_2O_2 production was redirected by the CN-CPDs hybrid system through three interrelated mechanistic factors. First, CPDs were inferred to lack nitrogen-coordinated metal centers, such as Fe-N_x, which were considered essential for efficient ORR on intrinsic g-C_3N_4 [48]. This structural deficiency was considered to result in suboptimal adsorption and desorption of ORR intermediates. The introduction of CPDs was found to alter the density and properties of the active sites, thereby shifting the ORR pathway from the desired $2e^-$ route ($O_2 + 2H^+ + 2e^- \rightarrow H_2O_2$) toward the competing $4e^-$ process ($O_2 + 4H^+ + 4e^- \rightarrow 2H_2O$). Consequently, the net yield of H_2O_2 was reduced. Second, the redox capability of the hybrid system was closely linked to its electronic structure. The CB potential was shifted negatively from −1.87 V to −1.29 V upon CPDs incorporation. This shift was considered to diminish the thermodynamic driving force for the reduction reactions, causing the H_2O_2 production rate to drop from 1704.2 to 477.6 $\mu mol \cdot g^{-1} \cdot h^{-1}$. Third, the reduced Fermi level was correlated with an increased energy barrier for the reaction between photogenerated electrons and O_2. This barrier was considered to retard the ORR kinetics. Thermodynamically, the lower Fermi level was argued to favor H_2 evolution rather than H_2O_2 accumulation, as the driving force for the $2e^-$ ORR was weakened relative to the proton reduction pathway. This kinetic and thermodynamic imbalance was considered to delay electron transfer to the active sites and ultimately suppress the overall ORR rate. Overall, the diminished H_2O_2 yield on the CN-CPDs hybrid was attributed to the combined effects of altered active site chemistry, unfavorable electronic band structure, and competing reaction pathways.

4 Conclusions

In conclusion, CPDs integrated with g-C_3N_4 were demonstrated to function as the tunable molecular switch for pathway selectivity in photocatalysis. By varying the CPDs loading, the photocatalytic product selectivity was reversibly switched. The optimized CN-CPDs hybrid achieved a 5.4-fold enhancement in the H_2 evolution rate (2826.0 $\mu mol \cdot g^{-1} \cdot h^{-1}$), whereas the H_2O_2 production rate was suppressed by 72%. The origin of this switching behavior was elucidated through combined experimental and DFT studies. CPDs promoted light absorption, charge separation, and also reconfigured the adsorption energetics of the *OOH intermediate, thermodynamically steering the ORR from the $2e^-$ pathway (H_2O_2) toward the $4e^-$ pathway (H_2O). This work established a design principle that balanced interfacial thermodynamics and charge-transfer kinetics for selectivity control. Notably, the decreased H_2O_2 yield provided critical insights for future optimization of CPDs toward targeted selectivity. Beyond the current system, deliberate tuning of surface functional groups (e.g., carboxyl, amino, or hydroxyl moieties), heteroatom doping (such as N, S, or P incorporation), or controlled particle size and carbonization degree could effectively modulate the adsorption energetics of ORR intermediates and the band alignment of the hybrid system. Such strategies may recover the $2e^-$ ORR selectivity for H_2O_2 production when desired, while preserving the beneficial effects of CPDs on light absorption and charge separation. Overall, this work thus provides a generalizable framework for selectivity engineering in carbon-based hybrid photocatalysts and other multi-electron energy conversion systems.

Acknowledgements

This work is supported financially by the National Science Foundation of China (Nos. 22405263 and 22035001).

Declaration of conflicting interests

The authors declare no conflicting interests regarding the content of this article.

Data availability

All data needed to support the conclusions in the paper are presented in the manuscript and/or the Supplementary Materials. Additional data related to this paper may be requested from the corresponding author upon request.

Electronic Supplementary Material: Supplementary material (further details of the DFT computational details, SEM and TEM images, Mott-Schottky plots, O_2 adsorption configurations, and tables of photocatalytic activities, elemental analysis, and time-resolved PL decay lifetimes) is available in the online version of this article at https://doi.org/10.26599/NRE.2026.9120272.

References

[1] Zhang, X.; Ma, P. J.; Wang, C.; Gan, L. Y.; Chen, X. J.; Zhang, P.; Wang, Y.; Li, H.; Wang, L. H.; Zhou, X. Y. et al. Unraveling the dual defect sites in graphite carbon nitride for ultra-high photocatalytic H_2O_2 evolution. *Energy. Environ. Sci.* **2022**, *15*, 830–842.

[2] Uekert, T.; Kasap, H.; Reisner, E. Photoreforming of nonrecyclable plastic waste over a carbon nitride/nickel phosphide catalyst. *J. Am. Chem. Soc.* **2019**, *141*, 15201–15210.

[3] Wu, X. J.; Fan, X. T.; Xie, S. J.; Lin, J. C.; Cheng, J.; Zhang, Q. H.; Chen, L. Y.; Wang, Y. Solar energy-driven lignin-first approach to full utilization of lignocellulosic biomass under mild conditions. *Nat. Catal.* **2018**, *1*, 772–780.

[4] Meng, G. P.; Wei, S.; Li, N.; Yin, Y. H.; Dong, B.; Sun, S. H.; Hu, G. W.; Wang, H.; Wang, B. D. Multisite atomic-chlorine-passivation stabilizes perovskite interfaces for efficient H_2O_2 photosynthesis from seawater. *Nat. Commun.* **2026**, *17*, 3988.

[5] Shiraishi, Y.; Ueda, Y.; Soramoto, A.; Hinokuma, S.; Hirai, T. Photocatalytic hydrogen peroxide splitting on metal-free powders assisted by phosphoric acid as a stabilizer. *Nat. Commun.* **2020**, *11*, 3386.

[6] Sun, Y. Y.; Han, L.; Strasser, P. A comparative perspective of electrochemical and photochemical approaches for catalytic H_2O_2 production. *Chem. Soc. Rev.* **2020**, *49*, 6605–6631.

[7] Teng, Z. Y.; Zhang, Q. T.; Yang, H. B.; Kato, K.; Yang, W. J.; Lu, Y. R.; Liu, S. X.; Wang, C. Y.; Yamakata, A.; Su, C. L. et al. Atomically dispersed antimony on carbon nitride for the artificial photosynthesis of hydrogen peroxide. *Nat. Catal.* **2021**, *4*, 374–384.

[8] Wu, Q. Y.; Cao, J. J.; Wang, X.; Liu, Y.; Zhao, Y. J.; Wang, H.; Liu, Y.; Huang, H.; Liao, F.; Shao, M. W. et al. A metal-free photocatalyst for highly efficient hydrogen peroxide photoproduction in real seawater. *Nat. Commun.* **2021**, *12*, 483.

[9] Qiao, F. Photoelectrocatalytic hydrogen production: Hydrogen production principle, performance optimization strategy, application and prospect. *Nano Res. Energy* **2025**, *4*, e9120132.

[10] Zhang, C. X.; Zhou, Y. M.; Li, Y.; Yang, X.; Liu, K.; Ayyub, A.; Lim, K. H.; Zheng, W.; Xu, M. S.; Yang, W. L. et al. Polyol-solid surface/interface transesterification strategy to construct precise anatase/rutile TiO_2 hetero-phase junctions towards enhanced photocatalytic performance. *Energy Mater.* **2025**, *5*, 500116.

[11] Luo, J.; Liu, Y. N.; Fan, C. Z.; Tang, L.; Yang, S. J.; Liu, M. L.; Wang, M. E.; Feng, C. Y.; Ouyang, X. L.; Wang, L. L. et al. Direct attack and indirect transfer mechanisms dominated by reactive oxygen species for photocatalytic H_2O_2 production on g-C_3N_4 possessing nitrogen vacancies. *ACS Catal.* **2021**, *11*, 11440–11450.

[12] Jiang, Z. L.; Sun, W. M.; Shang, H. S.; Chen, W. X.; Sun, T. T.; Li, H. J.; Dong, J. C.; Zhou, J.; Li, Z.; Wang, Y. et al. Atomic interface effect of a single atom copper catalyst for enhanced oxygen reduction reactions. *Energy Environ. Sci.* **2019**, *12*, 3508–3514.

[13] Liu, Y.; Zhao, Y. J.; Wu, Q. Y.; Wang, X.; Nie, H. D.; Zhou, Y. J.; Huang, H.; Shao, M. W.; Liu, Y.; Kang, Z. H. Charge storage of carbon dot enhances photo-production of H_2 and H_2O_2 over Ni_2P/carbon dot catalyst under normal pressure. *Chem. Eng. J.* **2021**, *409*, 128184.

[14] Yan, B.; Gu, Q. F.; Cao, W. W.; Cai, B.; Li, Y. W.; Zeng, Z. P.; Liu, P.; Ke, Z. F.; Meng, S.; Ouyang, G. et al. Laser direct overall water splitting for H_2 and H_2O_2 production. *Proc. Natl. Acad. Sci. USA* **2024**, *121*, e2319286121.

[15] Wang, T. T.; Zhang, L.; Wu, J. B.; Chen, M. Q.; Yang, S. F.; Lu, Y. L.; Du, P. W. Few-layer fullerene network for photocatalytic pure water splitting into H_2 and H_2O_2. *Angew. Chem., Int. Ed.* **2023**, *62*, e202311352.

[16] Gu, Y. Y.; Wang, J. X.; Tang, Q. Q.; Wei, H. T.; Ning, J.; Lan, X. F.; Wang, X. F.; Li, X. H.; Jia, Y. G.; Wang, S. B. et al. Insights into substituent effects on the fundamental photocatalytic processes of covalent organic frameworks toward H_2 evolution and H_2O_2 production reactions. *ACS Catal.* **2024**, *14*, 11262–11272.

[17] Salman Nasir, M.; Zhao, Y.; Ye, H. T.; Wang, T.; Sheng, B. W.; Song, J.; Li, J. L.; Wang, P.; Wang, X. Q.; Huang, Z. et al. Efficient hole extraction and $^{\bullet}$OH alleviation by Pd nanoparticles on GaN nanowires in seawater for solar-driven H_2 and H_2O_2 generation. *Angew. Chem., Int. Ed.* **2025**, *64*, e202420796.

[18] Wang, L. C.; Cao, S.; Guo, K.; Wu, Z. J.; Ma, Z.; Piao, L. Simultaneous hydrogen and peroxide production by photocatalytic water splitting. *Chin. J. Catal.* **2019**, *40*, 470–475.

[19] Chen, S. Y.; Luo, T.; Li, X. Q.; Chen, K. J.; Fu, J. W.; Liu, K.; Cai, C.; Wang, Q. Y.; Li, H. M.; Chen, Y. et al. Identification of the highly active Co–N_4 coordination motif for selective oxygen reduction to hydrogen peroxide. *J. Am. Chem. Soc.* **2022**, *144*, 14505–14516.

[20] Dang, X. M.; Wu, S.; Gan, X. R.; Zhang, H. G.; Jiang, X.; Zhang, Y. B.; Zhao, H. M. Dual-channels heterojunction interface engineering for efficient hydrogen peroxide photoproduction. *Adv. Funct. Mater.* **2026**, *36*, e74965.

[21] Zhang, X.; Zhou, Q. X.; Li, C.; Su, H.; Chen, T. R.; Cui, P. X.; Ban, C. G.; Tao, Y.; Wang, J. X.; Jiang, Y. H. et al. Thermodynamic and kinetic modulation of artificial H_2O_2 photosynthesis via spatial control of redox catalytic sites. *J. Am. Chem. Soc.* **2026**, *148*, 11068–11080.

[22] Yang, F.; Feng, C. Y.; Zuo, S. W.; Wang, Q. X.; Wei, F.; Hu, M.; Ren, Y. F.; Liu, D. Z.; Li, W. L.; Wang, S. B. et al. Photocatalytic H_2O_2 production with >30% quantum efficiency via monovalent copper dynamics. *J. Am. Chem. Soc.* **2025**, *147*, 17112–17120.

[23] Xia, H. Y.; Sun, H. N.; Yang, D. Y.; Zhao, J. W.; Gao, G.; Wu, L.; Huang, L.; Jiang, X. E. Curvature-engineered steering of oxygen electroreduction pathways on single-atom catalysts. *Angew. Chem., Int. Ed.* **2026**, *65*, e3924995.

[24] Jiao, X. C.; Zheng, K.; Chen, Q. X.; Li, X. D.; Li, Y. M.; Shao, W. W.; Xu, J. Q.; Zhu, J. F.; Pan, Y.; Sun, Y. F. et al. Photocatalytic conversion of waste plastics into C_2 fuels under simulated natural environment conditions. *Angew. Chem., Int. Ed.* **2020**, *59*, 15497–15501.

[25] Wu, Q. Y.; Liu, Y.; Cao, J. J.; Sun, Y.; Liao, F.; Liu, Y.; Huang, H.; Shao, M. W.; Kang, Z. H. A function-switchable metal-free photocatalyst for the efficient and selective production of hydrogen and hydrogen peroxide. *J. Mater. Chem. A* **2020**, *8*, 11773–11780.

[26] Yap, F. M.; Sheng Ling, G. Z.; Su, B. J.; Loh, J. Y.; Ong, W.-J. Recent advances in structural modification on graphitic carbon nitride (g-C_3N_4)-based photocatalysts for high-efficiency photocatalytic H_2O_2 production. *Nano Res. Energy* **2024**, *3*, e9120091.

[27] Yin, H.; He, J.; Xiao, B.; Zhou, M.; Wang, W.; Cunha, J.; Chen, Z. X.; Hou, Z. H.; Zhang, T. Q.; Yu, Z. P. Advances and prospects of g-C_3N_4 in lithium–sulfur batteries. *Nano Res. Energy* **2024**, *3*, e9120138.

[28] Ma, P. J.; Zhang, X.; Wang, C.; Wang, Z. W.; Wang, K. W.; Feng, Y. B.; Wang, J. X.; Zhai, Y. D.; Deng, J. G.; Wang, L. H. et al. Band alignment of homojunction by anchoring CN quantum dots on g-C_3N_4 (0D/2D) enhance photocatalytic hydrogen peroxide evolution. *Appl. Catal. B: Environ.* **2022**, *300*, 120736.

[29] Liu, J.; Liu, Y.; Liu, N. Y.; Han, Y. Z.; Zhang, X.; Huang, H.; Lifshitz, Y.; Lee, S. T.; Zhong, J.; Kang, Z. H. Metal-free efficient photocatalyst for stable visible water splitting via a two-electron pathway. *Science* **2015**, *347*, 970–974.

[30] Xu, M. Y.; Shen, R. C.; Yan, Y. H.; Mo, Y. Y.; Wang, S.; Zhang, P.; Li, X. Concerted proton-electron transfer in an S-Scheme PTA/g-C_3N_4 heterojunction enables efficient H_2O_2 photocatalysis. *Adv. Funct. Mater.* **2026**, *36*, e27907.

[31] Mou, Z. G.; Lu, C.; Yu, K.; Wu, H.; Zhang, H.; Sun, J. H.; Zhu, M. S.; Cynthia Goh, M. Chemical interaction in nitrogen-doped graphene quantum dots/graphitic carbon nitride heterostructures with enhanced photocatalytic H_2 evolution. *Energy Technol.* **2019**, *7*, 1800589.

[32] Guo, H. Z.; Zhou, L.; Huang, K.; Li, Y. Q.; Hou, W. D.; Liao, H. G.; Lian, C.; Yang, S. W.; Wu, D. L.; Lei, Z. D. et al. Nitrogen-rich carbon dot-mediated n→π* electronic transition in carbon nitride for superior photocatalytic hydrogen peroxide production. *Adv. Funct. Mater.* **2024**, *34*, 2402650.

[33] Zeng, H.; Li, Z. H.; Li, G. S.; Cui, X. Q.; Jin, M. X.; Xie, T. F.; Liu, L. L.; Jiang, M. P.; Zhong, X.; Zhang, Y. W. et al. Interfacial engineering of TiO_2/Ti_3C_2 MXene/carbon nitride hybrids boosting charge transfer for efficient photocatalytic hydrogen evolution. *Adv. Energy Mater.* **2022**, *12*, 2102765.

[34] Chen, X.; Zhang, W. W.; Zhang, L. X.; Feng, L. P.; Zhang, C. X.; Jiang, J.; Yan, T. J.; Wang, H. Sacrificial agent-free photocatalytic H_2O_2 evolution via two-electron oxygen reduction using a ternary α-Fe_2O_3/CQD@g-C_3N_4 photocatalyst with broad-spectrum response. *J. Mater. Chem. A* **2020**, *8*, 18816–18825.

[35] Pan, J. Q.; Wang, P. H.; Wang, P. P.; Yu, Q.; Wang, J. J.; Song, C. S.; Zheng, Y. Y.; Li, C. R. The photocatalytic overall water splitting hydrogen production of g-C_3N_4/CdS hollow core-shell heterojunction via the HER/OER matching of Pt/MnO_x. *Chem. Eng. J.* **2021**, *405*, 126622.

[36] Han, M.; Lu, S. Y.; Qi, F.; Zhu, S. J.; Sun, H. Z.; Yang, B. Carbon dots-implanted graphitic carbon nitride nanosheets for photocatalysis: Simultaneously manipulating carrier transport in inter-and intralayers. *Solar RRL* **2020**, *4*, 1900517.

[37] Liu, Y. P.; Huang, Z. J.; Wang, X. Y.; Hao, Y. M.; Yang, J. X.; Wang, H.; Qu, S. N. Recent advances in highly luminescent carbon dots. *Adv. Funct. Mater.* **2025**, *35*, 2420587.

[38] Qu, D.; Liu, J.; Miao, X.; Han, M. M.; Zhang, H. C.; Cui, Z.; Sun, S. R.; Kang, Z. H.; Fan, H. Y.; Sun, Z. C. Peering into water splitting mechanism of g-C_3N_4-carbon dots metal-free photocatalyst. *Appl. Catal. B: Environ.* **2018**, *227*, 418–424.

[39] Li, L. Y.; Wu, X.; Yan, Z. K.; Wu, J.; Huang, C. S.; Qu, S. N. Photo-responsive carbon dots for pyroptosis-mediated anti-tumor application. *Responsive Mater.*, in press, DOI: 10.1002/rpm2.70067.

[40] Han, M.; Zhu, S. J.; Xia, C. L.; Yang, B. Photocatalytic upcycling of poly(ethylene terephthalate) plastic to high-value chemicals. *Appl. Catal. B: Environ.* **2022**, *316*, 121662.

[41] Zhang, H. Q.; Liu, Y. P.; Qu, S. N. Recent advances in photo-responsive carbon dots for tumor therapy. *Responsive Mater.* **2024**, *2*, e20240012.

[42] Han, M.; Kang, C. Y.; Qu, Z. X.; Zhu, S. J.; Yang, B. Surface molecule induced effective light absorption and charge transfer for H_2 production photocatalysis in a carbonized polymer dots-carbon nitride system. *Appl. Catal. B: Environ.* **2022**, *305*, 121064.

[43] Yang, H. F.; Li, C.; Liu, T.; Fellowes, T.; Chong, S. Y.; Catalano, L.; Bahri, M.; Zhang, W. W.; Xu, Y. J.; Liu, L. J. et al. Packing-induced selectivity switching in molecular nanoparticle photocatalysts for hydrogen and hydrogen peroxide production. *Nat. Nanotechnol.* **2023**, *18*, 307–315.

[44] Barbieri, M.; Doardo, M.; Fortunati, I.; Fortunato, A.; Collini, E.; Arcudi, F.; Đorđević, L. Controlled aggregation of pyrene-based supramolecular nanostructures for light-driven switchable H_2 or H_2O_2 production. *Adv. Funct. Mater.* **2026**, *36*, 2505835.

[45] Yoshida, K.; Shiraishi, Y.; Ichikawa, S.; Tanaka, S.; Hirai, T. Photocatalytic solar hydrogen peroxide production on donor+acceptor linear polymer semiconductor powders reconfigurable by H-bonding and π-stacking interactions. *Angew. Chem., Int. Ed.* **2026**, *65*, e1682982.

[46] Feng, C. Y.; Tang, L.; Deng, Y. C.; Wang, J. J.; Luo, J.; Liu, Y. N.; Ouyang, X. L.; Yang, H. R.; Yu, J. F.; Wang, J. J. Synthesis of leaf-vein-like g-C_3N_4 with tunable band structures and charge transfer properties for selective photocatalytic H_2O_2 evolution. *Adv. Funct. Mater.* **2020**, *30*, 2001922.

[47] Cong, Y. Q.; Li, X. Y.; Zhang, S. Y.; Zheng, Q. A.; Zhang, Y.; Lv, S. W. Embedding carbon quantum dots into crystalline polyimide covalent organic frameworks to enhance water oxidation for achieving dual-channel photocatalytic H_2O_2 generation in a wide pH range. *ACS Appl. Mater. Interfaces* **2023**, *15*, 43799–43809.

[48] Jiang, W. J.; Gu, L.; Li, L.; Zhang, Y.; Zhang, X.; Zhang, L. J.; Wang, J. Q.; Hu, J. S.; Wei, Z. D.; Wan, L. J. Understanding the high activity of Fe–N–C electrocatalysts in oxygen reduction: Fe/Fe_3C nanoparticles boost the activity of Fe–N_x. *J. Am. Chem. Soc.* **2016**, *138*, 3570–3578.



Mei Han received her Ph.D. (2022) in Polymer Chemistry and Physics from the College of Chemistry, Jilin University under the supervision of Prof. Bai Yang. She joined the School of Materials Science and Engineering at Changchun University as a lecturer in January 2025. Her current research interests focus on the design, synthesis, and photocatalytic properties of carbon-based hybrid photocatalysts.



Bai Yang received his Ph.D. in Polymer Chemistry from Jilin University in 1991. He has been a Professor at Jilin University since 1994. He was awarded the National Science Fund for Distinguished Young Scholars and appointed as Cheung Kong Scholars Distinguished Professor in 1999. He has published over 800 papers with more than 54,000 citations and an H-index of 108, and has been continuously listed as a Highly Cited Researcher by Elsevier and Clarivate. He received the National Natural Science Award (Second Prize) in 2010. He is a Fellow of the Chinese Chemical Society and serves as an Associate Editor of *Green Carbon*. His research interests focus on polymer hybrids and photo-functional materials.